



Article

Microfluidic In-Situ Measurement of Poisson's Ratio of Hydrogels

Jean Cappello, Vincent d'Herbemont, Anke Lindner *  and Olivia du Roure

Laboratoire PMMH-ESPCI Paris, PSL Research University, Sorbonne Université, Université de Paris, 10, rue Vauquelin, F-75005 Paris, France; jean.cappello@espci.fr (J.C.); vincent.dherbemont@mines-paristech.fr (V.d.); olivia.duroure@espci.fr (O.d.R.)

* Correspondence: anke.lindner@espci.fr

Received: 21 February 2020; Accepted: 16 March 2020; Published: 19 March 2020

Abstract: Being able to precisely characterize the mechanical properties of soft microparticles is essential for numerous situations, from the understanding of the flow of biological fluids to the development of soft micro-robots. Here, we present a simple measurement technique for determining Poisson's ratio of soft micron-sized hydrogels in the presence of a surrounding liquid. This method relies on the measurement of the deformation, in two orthogonal directions, of a rectangular hydrogel slab compressed uni-axially inside a microfluidic channel. Due to the in situ character of the method, the sample does not need to be dried, allowing for the measurement of the mechanical properties of swollen hydrogels. Using this method, we determined Poisson's ratio of hydrogel particles composed of polyethylene glycol (PEG) and varying solvents fabricated using a lithography technique. The results demonstrate, with high precision, the dependence of the hydrogel compressibility on the solvent fraction and character. The method is easy to implement and can be adapted for the measurement of a variety of soft and biological materials.

Keywords: Poisson's ratio; hydrogels; microfluidics; PEG-DA; rheology

1. Introduction

Soft materials are found in situations as different as the flow of biological fluids, biomedical devices, micro-fluidic sensors, or soft micro-robotics, in forms such as soft polymeric particles or different types of protein or cell aggregates. Among soft materials, hydrogels are extremely powerful materials, allowing particles of controlled shapes to be manufactured at the micron scale. Their biocompatibility, softness, and easy and rapid fabrication make them perfectly suited for biomedical applications like drug delivery [1,2] or tissue engineering [3]. They are also useful as building blocks for the design of soft composite systems that are able to change shape in response to external stimuli, offering applications in soft robotics, flexible electronics, and biosensor development [4]. Being able to precisely characterize the mechanical properties of soft microparticles is essential when designing such applications, but faces specific problems due to their small scale, the dependence of their properties on the surroundings, and their ability to evolve over time.

The static linear mechanical properties of an isotropic elastic material are fully determined by two quantities: Young's modulus (E) and Poisson's ratio (ν). In a compressive test, Young's modulus links stress and strain, whereas Poisson's ratio quantifies the expansion of a material in directions perpendicular to the direction of compression. Poisson's ratio varies, for an isotropic material, from 0.5 (incompressible) to -1 . Other quantities such as the bulk modulus (K), the shear modulus (G), or Lamé's first coefficient (λ) correspond to different combinations of these two quantities [5].

Different techniques have been developed to measure Poisson's ratio. The most straightforward method relies on the measurement of the strain in two orthogonal directions during a compressive

test. Another method is to measure two different moduli, the bulk modulus K and Young's modulus E , and to obtain Poisson's ratio using their relationship $K = E/(3(1 - 2\nu))$. Classical methods usually require a macroscopic sample, and thus a significant volume of material, which can be limiting for microscopic soft particles. Additionally, in these classical methods the sample often needs to be fixed onto the testing apparatus and thus requires the sample to be dried [6]. For the soft materials considered here, drying may have a strong impact on the microstructure and thus on the material properties. In addition, soft hydrogels may have internal timescales due to poroelasticity and/or viscoelastic effects, which may influence their mechanical responses depending on the frequency or time scale of the chosen technique.

Some methods have been proposed to overcome these limitations. Wyss et al. [7] developed a simple method using microfluidics to measure the Poisson ratio of a soft particle relying on the independent measurement of the bulk and Young's modulus. However, the experimental errors of each of these measurements, even more pronounced for soft materials, limit the accuracy of the determination of Poisson's ratio, which only varies over a small range. Other techniques, such as micro-pipette aspiration experiments [8,9] or atomic force microscopy (AFM) [10], provide high-accuracy measurements of Poisson's ratio, but only locally probe the surface of the sample and do not provide bulk measurements. Acoustic waves can also be used to perform dynamic mechanical tests [11]. Usually the wave frequency varies from 0.5 to 5.0 MHz, and the measured elastic constants might be dependent on the frequency and differ from a static compression test. Finally, techniques such as small-angle X-ray scattering [12] also enable the measurement of Poisson's ratio, but require costly infrastructures.

In this article, we propose a simple and direct method to measure Poisson's ratio of soft hydrogels at long times directly inside a microchannel. We use a microfluidic setup where hydrogel particles are fabricated and subsequently transported in a channel whose width is smaller than the particle width (see Figure 1). After the full entry of the particle into the narrow channel, the external flow is stopped and the particle is solely submitted to an uniaxial compression by the lateral walls. This geometry is well adapted to determine Poisson's ratio by measuring at equilibrium the deformation of the particle in the direction of the uniaxial compression as well as in the perpendicular direction. As this method is performed in situ, no drying steps are required. This ensures that the structure of the material stays unmodified. Temporal observations of the hydrogel deformation allow for access to the time dependence of the process and to unequivocally determine the equilibrium state reached at long timescales. After detailing the method and its limitations we provide accurate measurements of Poisson's ratio of polyethylene glycol diacrylate (PEGDA) hydrogels fabricated in different solvents.

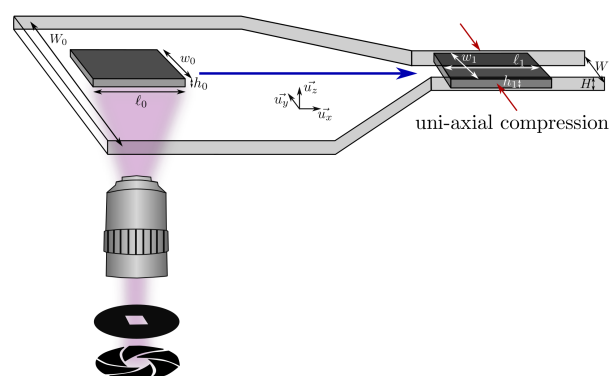


Figure 1. In situ fabrication of a particle using a microscope-based projection lithography technique. UV light is projected into a flat channel through a shutter and a rectangular mask resulting in the fabrication of a hydrogel particle surrounded by uncured solution. The slab is then pushed into a constriction by applying an external flow. When the particle has completely entered the narrow region of the channel the flow is stopped and the particle experiences uni-axial compression.

2. Materials and Methods

2.1. Channel and Particle Fabrication

PDMS (polydimethylsiloxane, Sylgard 184, DOWSIL) micro-channels were fabricated using traditional soft lithography techniques. The channels were bound to a glass slide covered with a thin layer of PDMS in order to have the same material on the four walls of the channel. The channels had a rectangular cross section and a constant height (either $H = 57 \pm 3 \mu\text{m}$ or $H = 103 \pm 3 \mu\text{m}$). They were composed of three regions: two linear channels with different width (a large channel on the order of millimeters and a small channel on the order of a few hundreds of micrometers) were connected by a constriction with a small angle (5 to 10 degrees).

Slabs of hydrogel with controlled geometry and position were directly fabricated inside the micro-channel using microscope-based photolithography [13]. This method has been extensively detailed in previous works [13–19], and just the essential steps are detailed here and schematically represented in Figure 1. The channel, filled with an oligomer solution and a photo-initiator, is exposed to a pulse of UV light of controlled duration. A mask with transparent drawings and black background is placed on the field-stop position of the microscope. The UV light passes through the mask and forms its image in the focal plane of the microscope. Thus, only the part of the channel corresponding to the transparent part of the drawings is illuminated by the UV light. Polymerization of the solution occurs in this region, allowing for the fabrication of hydrogel particles whose geometry corresponds to the drawings on the mask. After fabrication, the particles are surrounded by the uncured solution. The position of the particle only depends on the position of the channel relative to the objective of the microscope, which can be adjusted by moving the stage. Because the method of fabrication is based on a 2D projection technique, the 3D geometry of the particle results from the polymerization of the PEGDA in the height of the channel. The permeability of PDMS to oxygen (which inhibits the cross-linking reaction) leaves a non-polymerized lubrication layer of constant thickness on the top and bottom of the particles, allowing particles to be freely transported in the channel.

In this work, we used an inverted microscope (Zeiss Axio Observer) equipped with a UV light source (Lamp HBO 130 W) and a $\times 5$ Fluar objective. The shutter (Uniblitz, V25), with 10 ms response time, was coupled with an external generator (Agilent 33220A) and allowed for a very accurate control of the exposure time. We fabricated rectangular particles at zero flow rate in the wide region of the channel. The width w_0 and length ℓ_0 were determined by the dimensions of the drawings on the mask corrected with a factor that accounts for the objective magnification. The particle height is $h_0 = H - 2b$ where H is the channel height and b is the inhibition layer thickness (top and bottom), which we measured to be $b = 6 \pm 1.6 \mu\text{m}$. Due to the dimensions of the microchannel, the height of the fabricated particle was always smaller than its width and length. The maximal dimensions of a particle are set by the UV light beam diameter, and was 1.5 mm in our setup. To ensure homogeneous crosslinking of the hydrogel we chose to limit the maximal dimensions of the particle to 1 mm.

The photosensitive solution was composed of an oligomer, polyethylene glycol diacrylate (PEGDA, $M_n = 700 \text{ g/mol}$, Sigma), a photoinitiator (PI, 2-hydroxy-2-methylpropiophenone, Sigma), and a solvent. The solvent could be either pure water or a mixture of water and polyethylene glycol (PEG₁₀₀₀, $M_n = 1000 \text{ g/mol}$, Sigma) in a proportion of 1:2. While the proportion of solvent varied, the proportion of photoinitiator was kept constant at 10%. The volume fraction of water varied from 0% to 50%. Above 50% the solution became biphasic and no particle could be fabricated. The maximal dilution with the PEG₁₀₀₀:water mixture was 70%. Table 1 shows the composition of the different solutions used in this study.

Table 1. Volume fraction of each component of the different photosensitive solutions used in this study.

PEGDA	PI	Water	PEG ₁₀₀₀ :water Ratio 2:1 in Volume	Name
90%	10%	0%	0%	pure PEGDA
80%	10%	10%	0%	PW ₁₀
70%	10%	20%	0%	PW ₂₀
60%	10%	30%	0%	PW ₃₀
50%	10%	40%	0%	PW ₄₀
40%	10%	50%	0%	PW ₅₀
80%	10%	0%	10%	PP ₁₀
70%	10%	0%	20%	PP ₂₀
60%	10%	0%	30%	PP ₃₀
50%	10%	0%	40%	PP ₄₀
40%	10%	0%	50%	PP ₅₀
30%	10%	0%	60%	PP ₆₀
20%	10%	0%	70%	PP ₇₀

2.2. Experimental Protocol

The inlet of the micro-channel was connected to a reservoir, and a pressure controller (LineUP Series, Fluigent) was used to control the flow in the channel. Once the channel was filled with the photosensitive solution, the flow was stopped and a particle was fabricated. A picture of the particle was taken using a Hamamatsu Orca-flash 4.0 camera, which gave a precise measure of the dimensions before deformation (see Figure 2a). Then, the particle was pushed through the constriction into the narrow channel by imposing a flow through a pressure difference along the channel varying from a few hundred millibars to two bars. Once the particle had entirely entered the narrow region, the flow was turned off. There, the particle experienced uniaxial compression from the channel's lateral walls and we monitored its shape evolution with a frame rate of one image per second. Using standard image treatment procedures (with ImageJ [20] and MatLab), we extracted the shape of the particle before and during deformation and measured the particle width and length (see Figure 2c,d). The length of the compressed particles decreased from its initial value to an equilibrium value (see Figure 2e). In all our experiments we made sure to wait long enough (~ 1200 s) to measure the length ℓ_1 of the particle when this equilibrium was reached. At the end of the experiment, the particle was ejected from the narrow channel by again imposing a pressure-driven flow. We repeated this procedure at least 10 times for each condition. In some cases, at the end of the experiment, the particle was transported back into the wide channel where the particle shape was measured after the flow was stopped. We observed no residual deformation, confirming the reversibility of the deformation and ruling out any permanent deformations.

We varied the particle height ($h_0 = 45 \pm 3 \mu\text{m}$ and $h_0 = 91 \pm 3 \mu\text{m}$) and width ($w_0 = 205 - 470 \mu\text{m}$) and the narrow channel width ($W = 175 - 370 \mu\text{m}$). We kept the length of the particle constant and equal to $\ell_0 = 960 \pm 8 \mu\text{m}$. As can be seen in Figure 2b, the narrow channel was slightly deformed by the presence of the particle. We thus chose not to consider the width of the deformed particle to be equal to the width of the narrow channel but rather to measure w_1 for each experiment. The particle width w_1 differed only slightly from the channel width W and the importance of the difference between the two measures is given by the ratio of the Young modulus of the PDMS ($E_{PDMS} \sim 2 \text{ MPa}$ [21]) and the hydrogel [18]. Particle deformation in the y -direction will thus in the following be determined as w_0/w_1 instead of w_0/W .

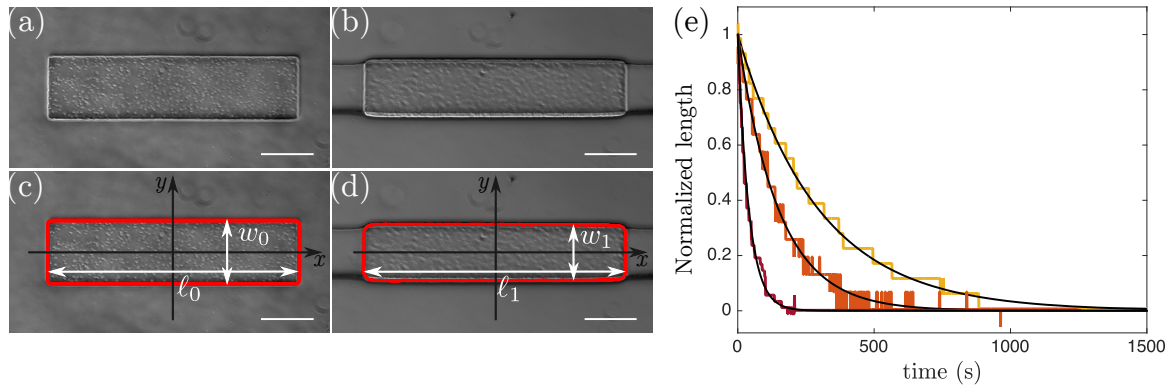


Figure 2. Pictures of the slab in the wide (a,c) and in the narrow (b,d) part of the channel. (a,b) correspond to raw images of the undeformed and deformed particle, respectively. In (b) the dark region around the particle corresponds to the channel walls. (c,d) show the determination of the shape using MatLab. Scale bars are 200 μm . (e) Temporal evolution of the particle length after the flow was stopped ($t = 0$). Length at time t was normalized by subtracting the equilibrium length and dividing by the difference between the initial length and the final length. Three different hydrogels are represented: from right to left, PP₂₀ (yellow), PP₃₀ (orange), and PP₄₀ (red). Exponential fits (black lines) are represented as a guide for the eyes.

2.3. Analysis

After the full entry of the particle into the narrow channel, the external flow was stopped and the particle was only submitted to an uniaxial compression by the lateral walls. We assumed that the hydrogel was isotropic and homogeneous and linear elasticity thus gives:

$$\epsilon_{xx} = \frac{1}{E} [(1 + \nu)\sigma_{xx} - \nu(\sigma_{xx} + \sigma_{yy} + \sigma_{zz})], \tag{1}$$

$$\epsilon_{yy} = \frac{1}{E} [(1 + \nu)\sigma_{yy} - \nu(\sigma_{xx} + \sigma_{yy} + \sigma_{zz})], \tag{2}$$

$$\epsilon_{zz} = \frac{1}{E} [(1 + \nu)\sigma_{zz} - \nu(\sigma_{xx} + \sigma_{yy} + \sigma_{zz})], \tag{3}$$

with σ and ϵ respectively being the stress and strain tensors of the particle. Equations (1) to (3) give the expression of the diagonal terms of σ and ϵ . E is the Young modulus of the hydrogel and ν is its Poisson ratio.

For the particle being submitted to a uniaxial compression in the y -direction, one can write $\sigma_{yy} = -P_{wall}$ and $\sigma_{xx} = 0$. Assuming that the deformed particle does not touch the top and bottom walls (i.e., $h_1 < H$) there is no stress in the z -direction and $\sigma_{zz} = 0$. This last assumption has to be verified a posteriori by evaluating the strain in the z -direction.

Equations (1)–(3) then become :

$$\epsilon_{xx} = -\frac{\nu}{E}\sigma_{yy}, \quad \epsilon_{yy} = \frac{1}{E}\sigma_{yy}, \quad \text{and} \quad \epsilon_{zz} = -\frac{\nu}{E}\sigma_{yy}. \tag{4}$$

The strains ϵ_{xx} and ϵ_{yy} are related to the changes of particle length and width

$$\epsilon_{yy} = \ln\left(\frac{w_1}{w_0}\right), \quad \epsilon_{xx} = \ln\left(\frac{l_1}{l_0}\right), \tag{5}$$

and Poisson’s ratio is directly given by their ratio:

$$\nu = -\frac{\epsilon_{xx}}{\epsilon_{yy}} = -\frac{\ln(l_1/l_0)}{\ln(w_1/w_0)}. \tag{6}$$

3. Results and Discussion

3.1. Validation of the Method

When the particle was compressed by the channel walls its length increased, as can be seen in Figure 2a–d, as expected for an elastic material. Figure 3 summarizes experiments where particles were created in a PW₃₀ solution and compressed into a channel of constant width $W = 175 \pm 0.7 \mu\text{m}$. The initial particle width w_0 was varied to apply varying confinements w_0/W . To extract Poisson's ratio we computed the ratio $-\epsilon_{xx}/\epsilon_{yy}$ according to Equations (6) taking into account that the width of the deformed particles was slightly different from the width W of the channel as a consequence of the deformation of the lateral channel walls (bottom of Figure 3a). Figure 3b summarizes our measurements of ν for different values of the confinement w_0/W . Each data point (blue circles) corresponds to one compressed particle and the average values and corresponding error bars are represented in dark blue. Larger w_0/W induces stronger deformation and thus larger stresses applied by the walls on the particle. In Figure 3b, Poisson's ratio is independent of w_0/W in the range [1 1.53] corresponding to the applied strain varying from -6.2% to -17.7% , validating our technique to measure a material property which is expected to be independent of the geometry, the applied stress, and the resulting strain. For very small ratios w_0/W ($w_0/W \leq 1.2$, light gray region) particle deformation was small and large scatter of the data points was observed. For the widest particle ($w_0 = 300 \mu\text{m}$), the stress was large enough to induce buckling (see the images in Figure 4a,b leading to a saturation of ℓ_1 and preventing any measurement of Poisson's ratio).

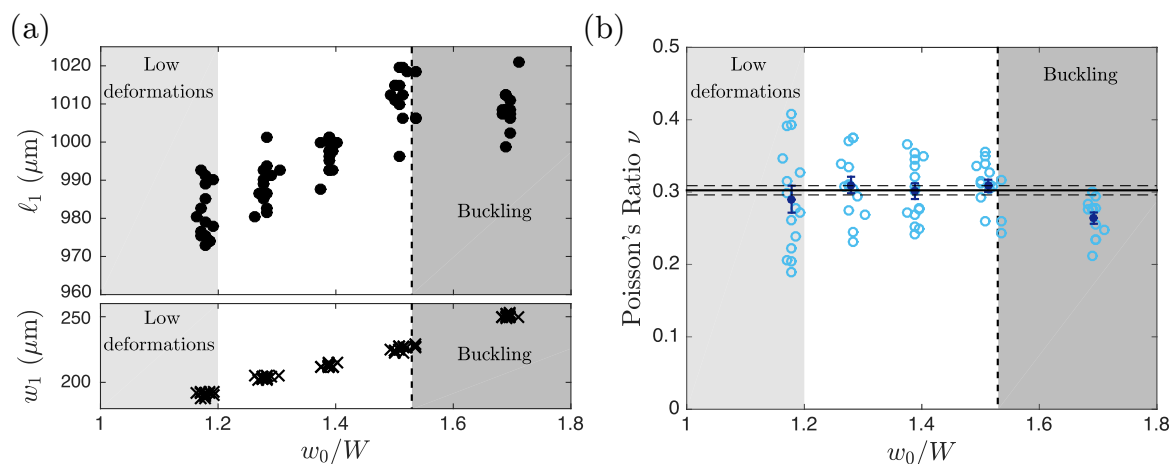


Figure 3. Direct measurements of particle length and width and the derivation of Poisson's ratio. Results are shown for the hydrogel PW₃₀ in a channel of width $W = 175 \pm 0.7 \mu\text{m}$ and height $H = 103 \pm 3 \mu\text{m}$. The initial particle length was kept constant $l_0 = 960 \pm 8 \mu\text{m}$ while the confinement w_0/W was increased. (a) Length (top) and width (bottom) of the deformed particle at equilibrium as a function of the confinement w_0/W . (b) Evolution of Poisson's ratio as a function of w_0/W . In (a,b) the light (dark) gray regions correspond to particle widths that are too small (large) to ensure good precision of the determination of Poisson's ratio. The vertical dotted line corresponds to the buckling threshold (see text). In (b) each light-blue circle corresponds to a single experimental measurement, and dark blue markers correspond to their average and standard deviation σ normalized by \sqrt{n} with $n = 15$ independent measurements. The horizontal black lines correspond to the average (solid line) and standard deviation (dashed line) of all points except from the dark gray region ($w_0/w_1 \geq 1.53$). Poisson's ratio was found to be $\nu_{30\%} = 0.302 \pm 0.007$ for the photosensitive solution PW₃₀.

3.2. Limitations

Limitations are inherent to every technique and it is essential to take them into consideration when developing a new method. In the following section, we discuss the range of validity for our microfluidic technique. First, our analysis relies on the assumption that the compressive stress was

solely applied in the y -direction by the lateral walls of the narrow channel and thus the only stress component that was non-zero was σ_{yy} . For this to be true deformation in the vertical direction needs to be small enough so that the particle does not touch the channel top and bottom walls, which would lead to an additional compressive stress σ_{zz} in the z -direction. This can be verified by comparing the height of the compressed particle to the channel height. The height of the deformed particle is $h_1 = h_0 \exp(\epsilon_{zz}) \sim h_0(1 - \nu\epsilon_{yy})$ and the condition $\sigma_{zz} = 0$ is verified as long as $-h_0\nu\epsilon_{yy} < 2b$. As a consequence the assumption is more likely to be verified for particles of small height h_0 and for small deformations. In all our experiments we verified a posteriori that the deformed particle height remained smaller than the channel height and thus that the assumption $\sigma_{zz} = 0$ was valid. We disregarded experiments where this was not the case. Note also that the condition $\sigma_{xx} = 0$ was not strictly verified close to the edges of the hydrogel particle due to the slight deformation of the PDMS channel (see Figure 2b,d). This effect is more important for particles of large elastic modulus and strong compression ϵ_{yy} , but is considered to be a small correction for our experiments.

Second, for too-small confinements w_0/W particle deformation was small and the experimental accuracy of ν was limited by the resolution of the deformed particle dimensions. The resolution could be improved either by applying stronger confinement (increasing the ratio w_0/W) or by upscaling the experiment, increasing both w_0 and W . However, we will see below that this can favor buckling instabilities and is thus not a favorable option in all cases.

Third, when the slab is too wide buckling may occur, preventing the measurement of Poisson's ratio. The critical stress to induce buckling in a thick elastic plate is given by $\sigma_{yy}^{crit} = \alpha\pi^2 \frac{E}{12(1-\nu^2)} \left(\frac{h_0}{w_0}\right)^2$ [22,23]. The correction factor α depends on the ratio w_0/h_0 and takes into account the shear deformation in the height. According to [23], $\alpha = 2.11$ for $w_0/h_0 = 2$ and $\alpha = 1.03$ for $w_0/h_0 = 10$. This critical stress is compared to the stress exerted by the lateral walls assuming linear deformation, $\sigma_{yy} = \epsilon_{yy}E$, via the dimensionless number

$$N = \frac{12(1-\nu^2)}{\alpha\pi^2} \left(\frac{w_0}{h_0}\right)^2 \epsilon_{yy}. \quad (7)$$

If $N > 1$ the particle buckles and, on the contrary, if $N < 1$ the particle deforms linearly. The black vertical dotted line in Figure 3 corresponds to $N = 1$ and good agreement between the theoretically predicted buckling threshold and the experimental observations was obtained. Buckling of the hydrogel particle was visible by direct observation (see Figure 4a,b) but also from the saturation of ℓ_1 at strong confinement (see Figure 3a) associated to the non-physical decrease of ν seen in Figure 3b. Since the buckling threshold N depends on Poisson's ratio as $1 - \nu^2$, variations of ν between 0 and 0.5 induce only very small modifications of N . Thus, the buckling threshold is mainly given by the geometry of the particle (via the particle aspect ratio w_0/h_0) and the geometry of the channel (the strain ϵ_{yy} being proportional to w_0/W). In conclusion, to avoid buckling, small $\epsilon_{yy} \propto w_0/W$ and small aspect ratios (w_0/h_0) are favorable.

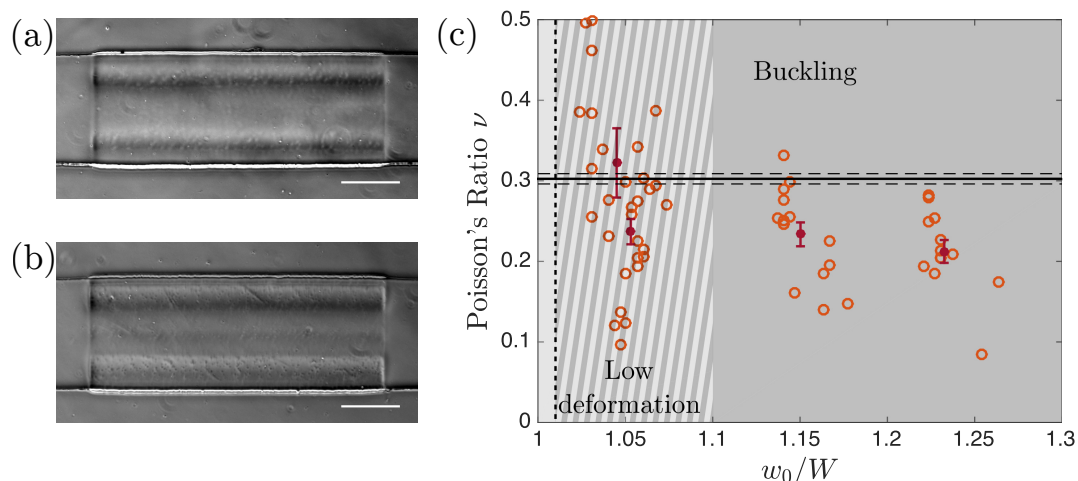


Figure 4. Limitations of the method. Results correspond to experiments performed with hydrogel particles created with the PW₃₀ photosensitive solution in a channel of width $W = 370 \pm 1 \mu\text{m}$ and height $H = 57 \pm 3 \mu\text{m}$. (a,b) show two pictures of buckled particles, at least two wavelengths are visible in (a) and three in (b). They correspond respectively to $w_0/W = 1.23$ and $w_0/W = 1.36$. (c) Evolution of the ratio $-\epsilon_{xx}/\epsilon_{yy}$ as a function of w_0/W . Open circles represent the results of single experiments and dark red markers represent average values of the different experiments. The light/dark gray regions of Figure 3b overlap for this example. Note that here also the measured ratio $-\epsilon_{xx}/\epsilon_{yy}$ is lower than Poisson's ratio when the particle buckles.

To illustrate these findings, in Figure 4c both the channel width and height were modified compared to Figure 3 while keeping the same photosensitive solution. The channel width W was increased to have a better resolution and the limit of the light grey region was indeed pushed to a lower value of w_0/W (≈ 1.1 to be compared to ≈ 1.2 in Figure 3b). The channel width on the other side was increased and the particles were thus more prone to buckle. The limit of the dark grey region was shifted to smaller values of w_0/W (≈ 1.01 compared to ≈ 1.53 in Figure 3b). As can be seen in the figure, despite the better resolution, the two grey regions overlap, meaning that this channel geometry does not allow for Poisson's ratio measurements.

The comparison of Figures 3b and 4c illustrates the compromise that has to be made between increasing the resolution on the particle deformation and avoiding particle buckling. A decrease of w_0 , keeping h_0 constant, increases the range of deformation before buckling but at the same time decreases the resolution. On the other hand, an increase of h_0 alone is favorable to avoid buckling but should be limited to prevent the deformed particle from touching the top and bottom walls. While designing channels for such measurements, one has to keep these two opposite effects in mind and to choose the best geometry varying the channel width and height accordingly.

Finally, for very soft particles and thus weakly crosslinked hydrogel particles (PP₆₀ and PP₇₀ [18]), we observed a dependency of the equilibrium length (ℓ_1) on the velocity at which a particle enters into the constriction. A possible reason for this observation can be found in the viscoelastic properties of the gel and/or the complex friction between the hydrogel and the lateral channel walls [24]. In such situations we consider that the measurement of Poisson's ratio cannot be achieved properly.

3.3. Dependence of Poisson's Ratio on the Solvent Composition

Using our method we measured Poisson's ratio of hydrogels fabricated from different compositions of photosensitive solutions with different solvent concentrations and solvent nature. Figure 5 shows the measured Poisson's ratio for dilutions of PEGDA $M_n = 700$ g/mol with water (blue points) and with a PEG₁₀₀₀:water mixture (2:1 in volume, purple points). In the absence of solvent the hydrogel was nearly incompressible ($\nu_{0\%} = 0.50 \pm 0.01$) which is in agreement with the literature [25]. In the presence of solvent, the hydrogel became compressible, as shown by the

decrease of Poisson's ratio. This compressibility results from the flow of solvent molecules leaving the particle when the hydrogel is compressed and depends on the microstructure of the cross-linked polymeric chains of PEGDA. Note that the hydrogel particles are incompressible during an isotropic compression imposed by a static pressure, as a consequence of the incompressibility of water. For larger dilution of the photosensitive solution, the fraction of solvent increases, leading to a smaller Poisson's ratio. In addition, we observed that for the same dilution, Poisson's ratio was always smaller in PEG₁₀₀₀:water compared to pure water. In water, the lowest value measured was $\nu_{50\%} = 0.255 \pm 0.009$ while in PEG₁₀₀₀:water this value was $\nu_{50\%} = 0.165 \pm 0.002$. The decreased value of Poisson's ratio reported here is a signature of the modified microstructure of the hydrogels. Further work is however necessary to fully understand the impact of the presence of chains of PEG in the surrounding medium on the compressibility of the hydrogels. Several hypotheses can be proposed: first, the presence of PEG is known to increase the porosity of the hydrogel [26], which is expected to modify its mechanical properties. The presence of PEG chains probably also impacts the connectivity of the meshwork as well as the chemical potentials of the different species.

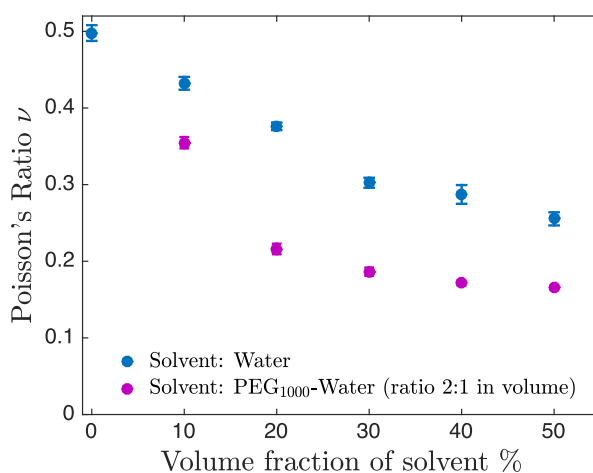


Figure 5. Evolution of the Poisson ratio of hydrogels fabricated from different photosensitive solutions as a function of the solvent volume fraction. Two different solvents are shown: water (blue markers) and a solution of PEG $M_n = 1000$ g/mol:water at a volume ratio of 2:1 (purple markers).

The flow of solvent through the polymeric mesh induced poroelastic effects, explaining the temporal evolution of the particle length shown in Figure 2e. Poroelasticity describes the flow of solvent through the mesh of a deformable material and introduces a time-dependent response to deformation. According to references [27,28] this poroelastic phenomenon is expected to depend on the porosity of the hydrogel and the viscosity of the solvent. The three different photosensitive solutions used in Figure 2e, PP₂₀ (yellow), PP₃₀ (orange), and PP₄₀ (red), have comparable viscosities ($\mu^{PP_{20}} = 108 \pm 3$ mPa·s, $\mu^{PP_{30}} = 107 \pm 3$ mPa·s, and $\mu^{PP_{40}} = 116 \pm 3$ mPa·s). On the contrary, the mesh size decreased with increasing dilution as the polymer chains were further apart during crosslinking in the presence of solvent molecules. This is in good agreement with the tendency shown in Figure 2e in which the characteristic relaxation time decreased when the solvent fraction increased. Note that as the poroelastic timescale also depends on the dimensions of the hydrogel, the timescales for micron-scale particles as in the present study are much smaller than for macroscopic particles [27,28]. Let us state again that all our measurements were performed at equilibrium to prevent any impact of these temporal effects on our measurement of the hydrogel compressibility.

4. Conclusions

Until now we have considered homogeneous materials and shown that our experimental technique is well-suited to determine the Poisson ratio of the material they are made of. Figure 6 shows the extension of our technique to metamaterials in which the geometry of the structure changed the

mechanical properties. In this example, an auxetic particle was fabricated using a specific design of the structure [29]. The superposition of the shapes of this particle before (gray) and after (black) introduction into the narrow channel clearly shows that the particle was slightly shorter when compressed, which is the signature of a negative Poisson's ratio.

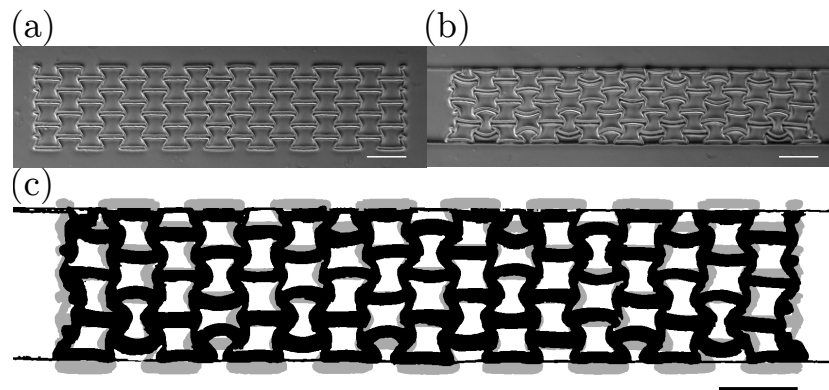


Figure 6. Auxetic metamaterial fabricated from a solution of 90% PEG-DA $M_n = 700$ g/mol and 10% photo-initiator in volume. (a) Before compression, (b) submitted to an uniaxial compression, (c) superposition of the undeformed and deformed shapes. The particle width and length decreased when compressed, which is indicative of a negative Poisson's ratio.

We presented a new technique for the measurement of Poisson's ratio of micrometric soft hydrogels with a very good measurement accuracy. The absolute measurement errors varying from 0.002 to 0.012 are comparable to what is obtainable using X-ray diffraction [12], and are much smaller than for measurements relying on the determination of two independent elastic moduli [7,30]. We successfully used this approach to measure Poisson's ratios of different hydrogels and showed that this Poisson ratio varied in a large range of values (0.165 to 0.5). We discussed the limitations of the methods and showed how channel and particle geometries should be chosen to accurately measure Poisson's ratio. Compared to other approaches, an important advantage of our method is that it is done in situ directly in the surrounding fluid and does not require any drying of the sample. Another advantage as compared to atomic force microscopy (AFM), which probes the mechanical properties at the nanometer scale, is the determination of the mechanical property (Poisson's ratio in our case) of the entire hydrogel particle on a scale much larger than the pore sizes even for very porous materials. Moreover, the technique presented here allows for an excellent measurement of the dynamical response of the material, enabling the determination of Poisson's ratio at long times and thus at equilibrium. Our characterization method is not limited to particles directly fabricated inside a microchannel but can also be used, for example, for protein or cell aggregates that can be flown into the microchannel. However, their potentially more complex shape and porosity can make the analysis less straightforward [31] and would require the use of effective strains and stresses to describe the particle deformation [32]. Moreover, if the condition $\sigma_{zz} = 0$ is not verified, our method could be adapted to measure Poisson's ratio, which in that case derives from the formula $\nu/(1 - \nu) = -\epsilon_{xx}/(\epsilon_{yy} + \epsilon_{zz})$. Because of these advantages and its simplicity, we believe that this method will be used for the characterization of Poisson's ratio of many different soft objects from nature and industry.

Author Contributions: J.C., V.d., A.L., and O.d.R. designed the study; J.C. and V.d. performed the experiments. J.C, A.L., and O.d.R. treated and analyzed the data. J.C, A.L., and O.d.R. wrote the paper. All authors have read and agreed to the published version of the manuscript.

Funding: This research was funded by the European Research Council through a consolidator grant (ERC PaDyFlow 682367). This work received the support of Institut Pierre-Gilles de Gennes (Équipement d'Excellence, "Investissements d'Avenir", Program ANR-10-EQPX-34).

Acknowledgments: We thank Al Crosby for inspiring discussions and Charles Duchêne for help with the experimental set-up.

Conflicts of Interest: The authors declare no conflicts of interest.

References

1. Nayak, S.; Lee, H.; Chmielewski, J.; Lyon, L.A. Folate-mediated cell targeting and cytotoxicity using thermoresponsive microgels. *J. Am. Chem. Soc.* **2004**, *126*, 10258–10259. [[CrossRef](#)]
2. Soppimath, K.S.; Tan, D.W.; Yang, Y.Y. pH-triggered thermally responsive polymer core–shell nanoparticles for drug delivery. *Adv. Mater.* **2005**, *17*, 318–323. [[CrossRef](#)]
3. Ambrosio, L.; De Santis, R.; Nicolais, L. Composite hydrogels for implants. *Proc. Inst. Mech. Eng. Part H J. Eng. Med.* **1998**, *212*, 93–99. [[CrossRef](#)]
4. Liu, Y.; Genzer, J.; Dickey, M.D. “2D or not 2D”: Shape-programming polymer sheets. *Prog. Polym. Sci.* **2016**, *52*, 79–106. [[CrossRef](#)]
5. Crandall, S.H.; Lardner, T.J.; Archer, R.R.; Cook, N.H.; Dahl, N.C. *An Introduction to the Mechanics of Solids*; McGraw Hill Science Engineering Math: New York, NY, USA, 1978.
6. Li, Y.; Hu, Z.; Li, C. New method for measuring Poisson’s ratio in polymer gels. *J. Appl. Polym. Sci.* **1993**, *50*, 1107–1111. [[CrossRef](#)]
7. Wyss, H.M.; Franke, T.; Mele, E.; Weitz, D.A. Capillary micromechanics: Measuring the elasticity of microscopic soft objects. *Soft Matter* **2010**, *6*, 4550–4555. [[CrossRef](#)]
8. Li, J. *Advances in Chemical Engineering: Characterization of Flow, Particles and Interfaces*; Academic Press: Cambridge, MA, USA, 2009; Volume 37.
9. Boudou, T.; Ohayon, J.; Picart, C.; Tracqui, P. An extended relationship for the characterization of Young’s modulus and Poisson’s ratio of tunable polyacrylamide gels. *Biorheology* **2006**, *43*, 721–728. [[PubMed](#)]
10. Hurley, D.C.; Turner, J.A. Measurement of Poisson’s ratio with contact-resonance atomic force microscopy. *J. Appl. Phys.* **2007**, *102*, 033509. [[CrossRef](#)]
11. Evans, K. *Measurement of Poisson’s Ratio*; Springer: Berlin, Germany, 1999; pp. 140–142.
12. Moram, M.; Barber, Z.; Humphreys, C. Accurate experimental determination of the Poisson’s ratio of GaN using high-resolution x-ray diffraction. *J. Appl. Phys.* **2007**, *102*, 023505. [[CrossRef](#)]
13. Dendukuri, D.; Panda, P.; Haghgoie, R.; Kim, J.M.; Hatton, T.A.; Doyle, P.S. Modeling of oxygen-inhibited free radical photopolymerization in a PDMS microfluidic device. *Macromolecules* **2008**, *41*, 8547–8556. [[CrossRef](#)]
14. Wexler, J.S.; Trinh, P.H.; Berthet, H.; Quennou, N.; du Roure, O.; Huppert, H.E.; Linder, A.; Stone, H.A. Bending of elastic fibres in viscous flows: The influence of confinement. *J. Fluid Mech.* **2013**, *720*, 517–544. [[CrossRef](#)]
15. Berthet, H.; du Roure, O.; Lindner, A. Microfluidic Fabrication Solutions for Tailor-Designed Fiber Suspensions. *Appl. Sci.* **2016**, *6*, 385. [[CrossRef](#)]
16. Duprat, C.; Berthet, H.; Wexler, J.S.; du Roure, O.; Lindner, A. Microfluidic in situ mechanical testing of photopolymerized gels. *Lab A Chip* **2014**, *15*, 244–52. [[CrossRef](#)] [[PubMed](#)]
17. Nagel, M.; Brun, P.T.; Berthet, H.; Lindner, A.; Gallaire, F.; Duprat, C. Oscillations of confined fibres transported in microchannels. *J. Fluid Mech.* **2018**, *835*, 444–470. [[CrossRef](#)]
18. Cappello, J.; Bechert, M.; Duprat, C.; du Roure, O.; Gallaire, F.; Lindner, A. Transport of flexible fibers in confined microchannels. *Phys. Rev. Fluids* **2019**, *4*, 034202. [[CrossRef](#)]
19. Bechert, M.; Cappello, J.; Daëff, M.; Gallaire, F.; Lindner, A.; Duprat, C. Controlling transport dynamics of confined asymmetric fibers. *arXiv* **2019**, arXiv:1903.00761.
20. Schneider, C.A.; Rasband, W.S.; Eliceiri, K.W. HISTORICAL commentary NIH Image to ImageJ : 25 years of image analysis. *Nat. Methods* **2012**, *9*, 671–675. [[CrossRef](#)]
21. Gervais, T.; El-Ali, J.; Günther, A.; Jensen, K.F. Flow-induced deformation of shallow microfluidic channels. *Lab A Chip* **2006**, *6*, 500–507. [[CrossRef](#)]
22. Jones, R.M. *Buckling of Bars, Plates, and Shells*; Bull Ridge Corporation: Blacksburg, VA, USA, 2006.
23. Onyia, M.E.; Rowland-Lato, E.O. Determination of the Critical Buckling Load of Shear Deformable Unified Beam. *Int. J. Eng. Technol.* **2018**, *10*, 647–657. [[CrossRef](#)]
24. Gong, J.P. Friction and lubrication of hydrogels—its richness and complexity. *Soft Matter* **2006**, *2*, 544–552. [[CrossRef](#)]

25. Gabler, S.; Stampfl, J.; Koch, T.; Seidler, S.; Schuller, G.; Redl, H.; Juras, V.; Trattnig, S.; Weidisch, R. Determination of the viscoelastic properties of hydrogels based on polyethylene glycol diacrylate (PEG-DA) and human articular cartilage. *Int. J. Mater. Eng. Innov.* **2009**, *1*, 3–20. [[CrossRef](#)]
26. Lee, A.G.; Arena, C.P.; Beebe, D.J.; Palecek, S.P. Development of macroporous poly (ethylene glycol) hydrogel arrays within microfluidic channels. *Biomacromolecules* **2010**, *11*, 3316–3324. [[CrossRef](#)] [[PubMed](#)]
27. Cai, S.; Hu, Y.; Zhao, X.; Suo, Z. Poroelasticity of a covalently crosslinked alginate hydrogel under compression. *J. Appl. Phys.* **2010**, *108*, 113514. [[CrossRef](#)]
28. Hu, Y.; Zhao, X.; Vlassak, J.J.; Suo, Z. Using indentation to characterize the poroelasticity of gels. *Appl. Phys. Lett.* **2010**, *96*, 121904. [[CrossRef](#)]
29. Ren, X.; Das, R.; Tran, P.; Ngo, T.D.; Xie, Y.M. Auxetic metamaterials and structures: A review. *Smart Mater. Struct.* **2018**, *27*, 023001. [[CrossRef](#)]
30. Punter, M.T.; Vos, B.E.; Mulder, B.M.; Koenderink, G.H. Poroelasticity of (bio) polymer networks during compression: Theory and experiment. *arXiv* **2020**, arXiv:1910.00490.
31. Duchêne, C.; Filipe, V.; Huille, S.; Lindner, A. Clogging of microfluidic constrictions by monoclonal antibody aggregates: Role of aggregate shape and deformability. *Soft Matter* **2020**, *16*, 921–928. [[CrossRef](#)]
32. Bommireddy, Y.; Agarwal, A.; Yettella, V.; Tomar, V.; Gonzalez, M. Loading-unloading contact law for micro-crystalline cellulose particles under large deformations. *Mech. Res. Commun.* **2019**, *99*, 22–31. [[CrossRef](#)]



© 2020 by the authors. Licensee MDPI, Basel, Switzerland. This article is an open access article distributed under the terms and conditions of the Creative Commons Attribution (CC BY) license (<http://creativecommons.org/licenses/by/4.0/>).